Sadia Ata, Sara Bano, Ismat Bibi*, Norah Alwadai, Ijaz ul Mohsin, Maryam Al Huwayz, Munawar Iqbal* and Arif Nazir

Cationic distributions and dielectric properties of magnesium ferrites fabricated by sol-gel route and photocatalytic activity evaluation

Abstract: Sol-gel auto combustion method was adopted to fabricate magnesium ferrite ($MgFe_2O_4$) nanoparticles. The structural and morphological properties was studied by XRD, FTIR, and SEM analysis. The average particle sizes of $MgFe_2O_4$ was in the range of 35–55 nm. The octahedral & Tetrahedral bond lengths, R_{AE} (tetrahedral edge length), R_{BE} (shared octahedral edge length) and R_{BEU} (individual octahedral edge length), cationic radii (tetra and octa-sites) were also determined. The magnetic strength also showed direct reliance on bond angle and indirect to bond length. Hoping length L_a and L_b and bond angles are also measured. The frequency dependent conductivity and dielectric properties of $MgFe_2O_4$ were investigated by Impedance analyzer. The photocatalytic activity (PCA) is appraised against MB (methylene blue) dye and $MgFe_2O_4$ calcined at 800 °C showed promising degradation (78%) under visible light irradiation. The findings revealed that $MgFe_2O_4$ is can harvest the solar light, which could be employed for the remediation of wastewater contains textile dyes.

Keywords: dielectric properties; environmental pollution; magnesium ferrite; nanoparticles; photodegradation methylene blue dye.

***Corresponding authors: Ismat Bibi**, Institute of Chemistry, The Islamia University of Bahawalpur, Bahawalpur, Pakistan, E-mail: drismat@iub.edu.pk; and **Munawar Iqbal**, Department of Chemistry, Division of Science and Technology, University of Education, Lahore, Pakistan, E-mail: bosalvee@yahoo.com

Sadia Ata and Sara Bano, School of Chemistry, University of the Punjab, Lahore, Pakistan

Norah Alwadai and Maryam Al Huwayz, Department of Physics, College of Sciences, Princess Nourah bint Abdulrahman University, P.O. Box 84428, Riyadh 11671, Saudi Arabia

Ijaz ul Mohsin, Institute of Applied Materials–Applied Materials Physics (IAM-AWP), Karlsruhe Institute of Technology, Karlsruhe, Germany

Arif Nazir, Department of Chemistry, The University of Lahore, Lahore, Pakistan

1 Introduction

The nano-ferrites preparation is attained much importance due to their ideal surface-to-volume ratio, which enable them to enhance the properties of the materials for diverse type of applications. The structures of matter could be modified by dominant individual atoms with the advancement of nanotechnologies [1, 2]. The materials synthesis/development of devices, through control of matter and exploitation of their properties on 1–100 nm scale have contributed abundant opportunities in field of science and technology [3–5]. Nanomaterials are playing a crucial role in every field of life because of their high surface energies, which needs exploration of distinctive characteristics. Mg ferrites NPs showed excellent physical and chemical properties such as superparamagnetic behavior, high magnetic porosity and low magnetic loss [6, 7]. $MgFe_2O_4$ NPs are superior over alternative electromagnetic materials attributable to their high electric resistance and stability over a temperature range [6]. These NPs are soft magnetic n-type semiconductors having applications in microwave devices, noise filters, magnetic storage devices, electrical device cores, drug delivery systems, cancer medical aid, resonance imaging (MRI) and contact action and Mg–ferrites have been successfully applied in different fields [8–11]. Being as economical catalyst, NPs are important photocatalyst for the treatment of wastewater. Typical use of ferrites is as photo-catalyst for degradation of pollutants in visible light. The low values of band gap of ferrites make them active under visible light. $MgFe_2O_4$ having energy gap of 2.18 eV, can be used as a catalyst. Synthesis technique of metal ferrites and calcination temperature have an effect on the properties, particle size and ion distribution of NPs [6, 7, 12]. Metal ferrites synthesized by auto-combustion sol-gel approach have spinel structure during in which Fe are placed in tetrahedral and octahedral sites, whereas Mg are located in octahedral sites. The torque entirely depends on ion distribution of iron, whereas magnesium ion is non-magnetic in nature. Ion distribution in mineral Mg–ferrite is extremely sensitive to temperature treatment and have an effect on the structural properties. Distribution of cations in crystal structure conjointly depend upon the derivatives of metal ferrites [13]. Different techniques like hydrothermal, co-precipitation and micro emulsion have been used for ferrites preparation. Each technique has influence on the structure, size, physical and chemical properties of NPs [14–17]. Based on a for mentioned facts, Mg ferrite NPs were synthesized via sol-gel auto combustion route and their cationic distribution, dielectric, structural, morphological, and photocatalytic properties were investigated in the present investigation.

2 Material and methods

2.1 Chemical and reagents

All the chemicals including $Mg(NO_3)_2.6H_2O$ (99%), $Fe(NO_3)_3.9H_2O$ (99%), citric acid (99%), ethylene glycol, methanol, ammonium hydroxide (28%), $C_{16}H_{18}ClN_3S.H_2O$ were obtained from Sigma-Aldrich and used without further purification. For solution preparation, Milli pure water was used throughout the study.

2.2 Synthesis procedure

Sol-gel auto combustion approach was adopted for the fabrication of Mg ferrites. Equal molar ratios of citric acid, magnesium and iron nitrates were mixed in 100 mL H_2O. Glycol was used as cooling agent and pH of the resultant mixture was adjusted at 7.0 using ammonium hydroxide [18]. Then the mixture was kept at 80 °C under constant stirring until gel was obtained. Temperature of gel was increased slowly up to 200 °C until combustion started and brown color powder was obtained. After washing, the drying of the resultant ferrites was done at 80 °C for 2 h and calcined at 700 °C and 800 °C for 3 h.

2.3 Photodegradation

Photocatalytic degradation of MB dye (10 mg/L) was investigated using Mg ferrite calcinated at 700 and 800 °C under visible light irradiation. Different parameters like effect of dose of photocatalyst and incubation time effect was also investigated on degradation efficiency. The mixture (solution of dye and catalyst) are placed for 25 min in dark before irradiation and then, irradiated to visible light (150 W Xe Lamp) for different time intervals and after stipulated time period, 2 mL sample was withdrawn, filtered and absorbance (CE Cecil 7200, UK) was measured 664 nm and dye removal (%) was calculated as depicted in Eq. (1) (C_0 and C_f are the absorbance at t zero and time "t," respectively).

$$\text{Degradation (\%)} = \frac{C_0 \quad C_f}{C_0} \text{ x } 100 \tag{1}$$

3 Results and discussion

3.1 XRD analysis

Figure 1 shows the XRD peaks at 2θ values of 30.083, 35.43, 43.04, 54.5 and 56.92° that corresponds to (511), (422), (400), (311), and (220) planes was observed, which revealed the formation of spinel structure and the synthesized material was crystalline in nature [19, 20]. It had been noted that crystallinity of ferrites was increased with temperature and these findings are in line with reported studies [21, 22]. Structural

studies of Mg–ferrite were appraised by analysing the lattice constant, particle size, strain, packing factor, dislocation density, tolerance factor, ion radii and iteration lengths using XRD data for as a function of calcination temperatures and results are depicted in Table 1. The results revealed that particle size decreased by increasing calcination temperature. The packing potency of unit volume of atoms dislocation density and strain for was calculated and it was observed that defects in crystal are often scale back at high calcination temperature [23]. The change in structural properties is due to the Mg ions, which occupy interstices which causes strain by decreasing lattice parameters and cell volume of cubic cell structure. A decrease in John-Teller distortion also causes compression distortion at octahedral site, which promote cubic crystalline structure [16]. The formula for spinel structure (inverse) for distribution of cations at tetrahedral and octahedral sites is depicted in Eq. (2).

$$\left[Mg_x^{2+}Fe_{1\ x}^{3+}\right]_A\left[Mg_{1\ x}^{2+}Fe_{1+x}^{3+}\right]_B O_4^2 \tag{2}$$

where, *A* provides ion distribution at tetrahedral sites and *B* gives distribution of cation at octahedral site. *O* particle is enclosed by four cations creating a tetrahedron that the separation between tetrahedral power cations (0, 0, 0) and *O* is (3/8, 3/8, 3/8) on the body diagonal that characterizes the proper estimation of *O* point parameter (u = 3/8). *O* point parameter is the distance of oxygen particle on the diagonal body. Once tetrahedral interstices are occupied by the particle than the enlargement in tetrahedral site is comparatively larger than octahedral site because of the distinction of ionic radii of cations and the distance of *O* atom on the body diagonal shift from ideal worth, which was calculated is shown in Table 2. Radii (R_a and R_b), octahedral and tetrahedral bond lengths, R_{AE}, R_{BE} and R_{BEU} values were calculated using X-ray diffraction data. Cationic radii for tetra and octa-sites were determined at different temperature and responses are shown Figure 2. The interaction (magnetic) between cations (B–B, A–B, A–A) or cations and anions (A–O, B–O) depends upon the bond (lengths & angles). The magnetic strength has direct reliance on bond angle and indirect on bond length. Hoping length L_a and L_b and bond angles are also calculable using XRD and also other structural parameters were also calculated using XRD data. Figure 3 shows the relation of crystallite size and packing fraction as a function of temperature. Figure 4 depicts the values of unit cell volume and X-ray density versus temperature (calcination). The value of unit cell volume and X-ray density (average) were found to be 589.448 Å^3 and 5.33884 g/cm^3, respectively and both parameters showed a inverse relation with respect to each other. There is small variations can be because of diverse dissemination of cations at the accessible sites. Dislocation density decreases linearly as temperature increases that gives the idea to minimize crystal defects. The acceptable range of oxygen positional parameter is 0.357 and a change may be due to divalent atoms (Mg^{+2}) ion at tetrahedral site having bigger radii as

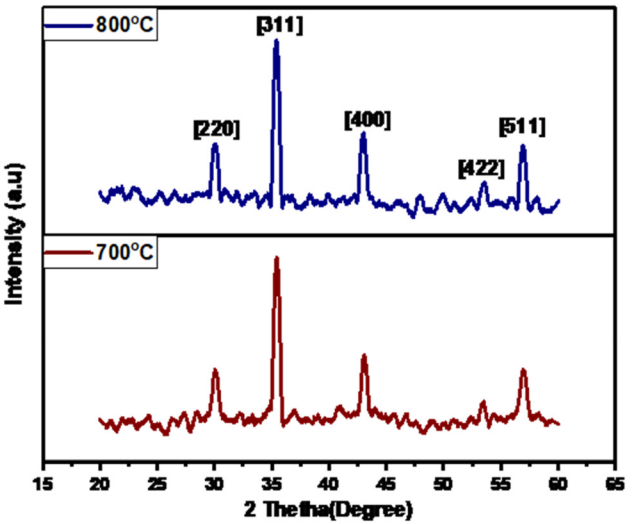

Figure 1A: XRD pattern of Mg ferrites calcined at 700 °C and 800 °C, respectively.

compared to Fe^{+3}. Variation between lattice constants and oxygen positional parameters was shown in Figure 5. The lattice constant values (theoretical and experimental) were found matching with each other (Figure 6) and a variation might occurs due to secondary phase presence of the ferrite. The tolerance factor for value

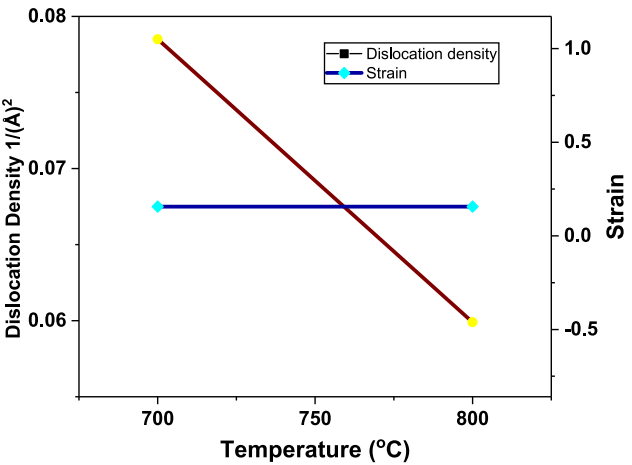

Figure 1B: Variation in strain and dislocation density for samples calcined at 700 °C and 800 °C.

Table 1: Different structural parameters of $MgFe_2O_4$ XRD data.

Parameters	Sample 1 calcined (700 °C)	Sample 2 calcined (800 °C)
a (Å)	8.423	8.423
D (nm)	35.51	46.96
V (Å^3)	591.01	591.01
d	2.5305	2.5305
ε	0.1561	0.1561
Δ	0.0785	0.0594
P	140.32	185.5
d_x (g/cm^3)	5.400	5.4

Table 2: Structural parameters of $MgFe_2O_4$ calculated by cationic distribution.

Parameters	Sample calcined (700 °C)	Sample calcined (800 °C)
a_{exp} (Å)	8.451	8.451
U	0.3902	0.3902
R_a	0.70752	0.70752
R_b	0.64624	0.64624
a_{theo}	8.40060	8.40060
T	1.0548	1.0548
<A–O>	2.03995	2.03995
<B–O>	1.97246	1.97246
R_{AE}	3.33101	3.33101
R_{BE}	2.60890	2.60890
R_{BEU}	2.974	2.974
L_a	3.3634	3.3634
L_b	2.96914	2.9614
b	2.9691	2.9691
c	3.48163	3.48163
d	3.6364	3.6364
e	5.4546	5.4546
f	5.1427	5.1427
p	1.97143	1.97143
q	2.04004	2.04004
r	3.9063	3.9063
s	3.71038	3.71038
Θ_1	120.425	120.425
Θ_2	133.523	133.523
Θ_3	97.709	97.709
Θ_3	126.94	126.94
Θ_4	67.115	67.115

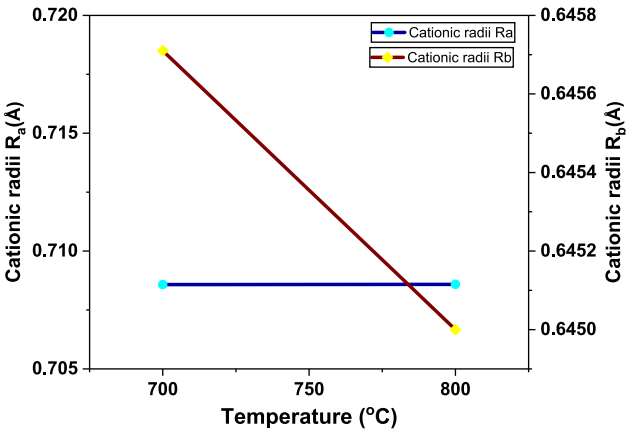

Figure 2: Variation in cation radii R_a and cation radii R_b for samples calcined at 700 °C and 800 °C.

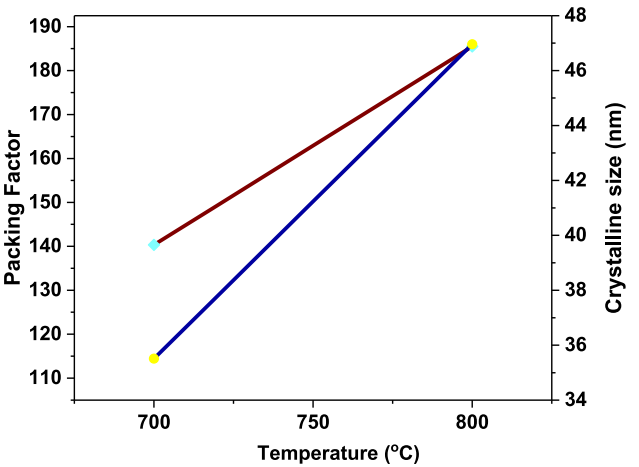

Figure 3: Variation in crystallite size and packing factor for samples calcined at 700 °C and 800 °C.

was equivalent to unity which confirm the cubic inverse spinel structure of the $MgFe_2O_4$ (Figure 7).

3.2 Surface morphology

The SEM analysis was employed to determine the morphology of the prepared NPs [24, 25] and images are shown in Figure 8 and Table 3, the average particle size was in

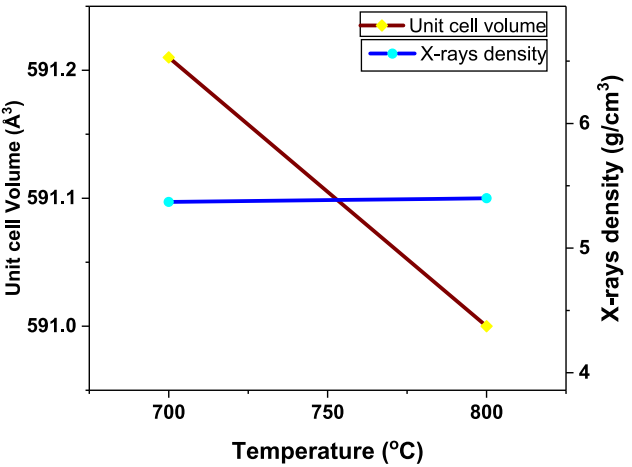

Figure 4: Variation in unit cell volume and X-ray density for samples calcined at 700 °C and 800 °C.

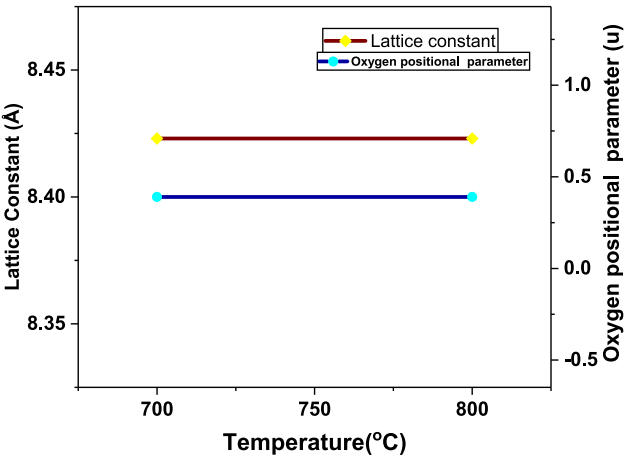

Figure 5: Variation in lattice constant and oxygen positional parameter for samples calcined at 700 °C and 800 °C.

45–55 nm range and spherical in shape. It is observed that there is difference in the particle sizes calculated by SEM and XRD using Scherrer's formula. These variations can be due to the difference in the size of ionic radii, alternation in molecular structure and lattice strain or clustering of fine NPs. Hence, the XRD method has a more accurate standards and estimation of sizes [18, 26]. SEM image of magnesium ferrite NPs calcined at 800 °C revealed polyhedral nature and is in line with previous reports [27].

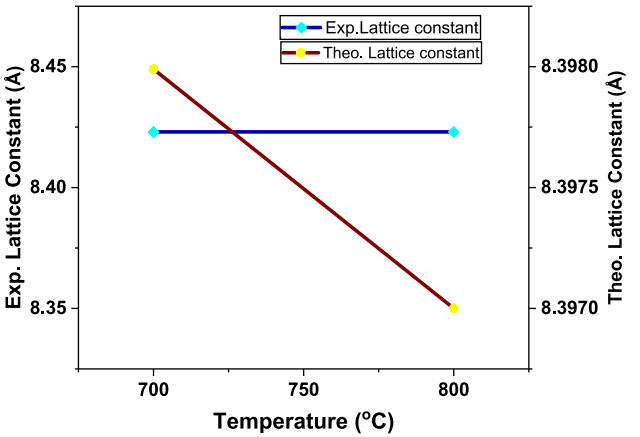

Figure 6: Variation in exp. lattice constant and Theo lattice constant for samples calcined at 700 °C and 800 °C.

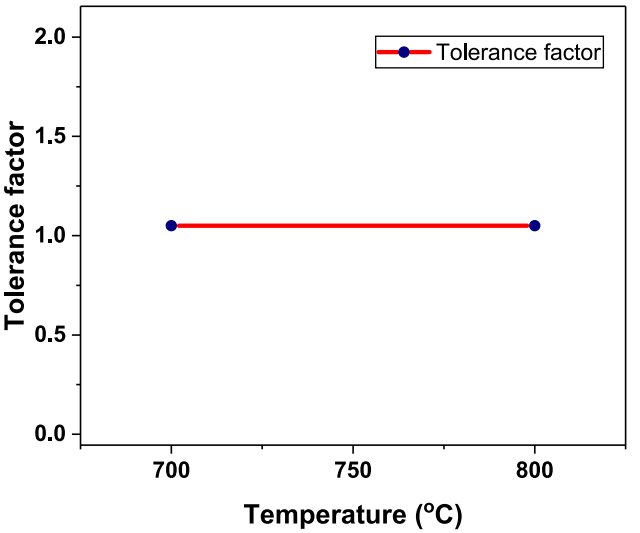

Figure 7: Tolerance factor of samples calcined at 700 °C and 800 °C.

3.3 FTIR analysis

The synthesized $MgFe_2O_4$ ferrite are also characterized by FTIIR spectroscopy for functional group identification [28, 29]. Samples calcined at different temperature

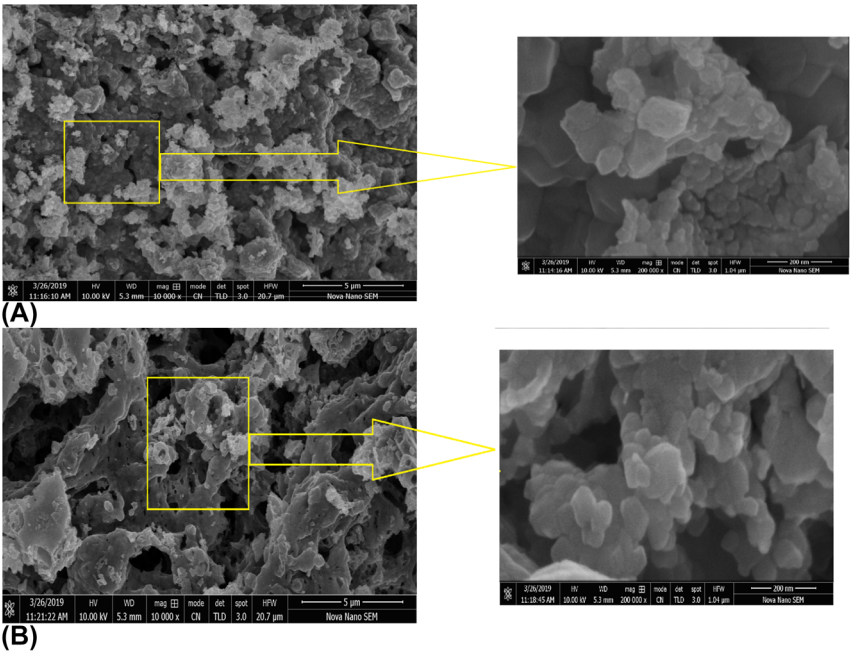

Figure 8: SEM micrographs of $MgFe_2O_4$ calcined at (A) 700 °C and (B) 800 °C.

Table 3: Average particle sizes of $MgFe_2O_4$ ferrite calcined at 700 °C (S1) to 800 °C (S2).

Sample	Temperature	*D* (nm) XRD	*D* (nm) SEM
S1	700 °C	35.51	46.881
S2	800 °C	46.96	55.732

shows peaks almost on same position which support the spinel structure of Mg ferrites. The peaks at 3421 cm^{-1} and 3400 cm^{-1} indicate the presence of water absorbed, it could be attributed to O–H stretching vibration of H_2O. The peak at 2337 cm^{-1} describes the H–O–H bending vibrations of the absorbed water. These peaks disappear when the samples were further annealed at higher temperature [18]. The bands in the range of 570 cm^{-1} to 472 cm^{-1} are assigned to deformation vibrations of Fe–OH group. There are metal oxygen bands are observed in the range of 560 cm^{-1} to 466 cm^{-1} confirmed the octahedral and tetrahedral sites of spinel ferrites. The typical low frequency band at around 562 cm^{-1} refers to Fe–O vibration (Fe^{3+} bond) in octahedral and tetrahedral sites and the band at around 473.25 cm^{-1}

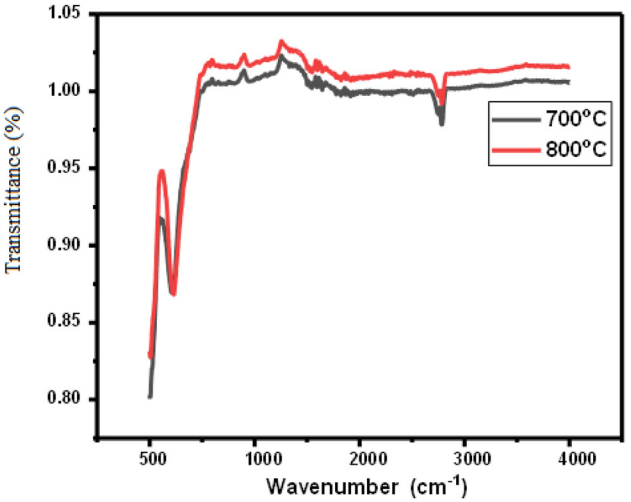

Figure 9: FTIR analysis of $MgFe_2O_4$ NPs calcined at 700 °C and 800 °C.

refers to Fe–O vibration (Fe^{2+} bond) in octahedral sites [30]. Shift of the peaks towards lower frequencies suggests reduced binding energy between the metal ion and the oxygen ions for smaller particle (Figure 9).

3.4 Dielectric properties

3.4.1 Dielectric constant

Dielectric constant of was appraise as depicted in Eq. (3). Where, C is the capacitance, d is thickness of pallet, A is the area of pellets and ε_0 is permittivity of free space.

$$\varepsilon' = CdA\varepsilon_0 \tag{3}$$

Changes in dielectric constant (ε') versus temperature in the relation of frequency is shown in the Figure 10. Frequencies values varies from 100 Hz to 20 MHz that make dispersion curve with ε'. Dielectric constant is decreased with the frequency and this change was sharp at initial stage and then, at higher frequencies it decreases slowly. In fact, the polarons not go behind the alternating electric field and other polarizations excluding electronic polarization become insignificant at high frequency and also, this observation correlates well with previous reports [30]. Maxwell-Wagner plot was detected when the trend of dielectric constant of all the observable samples was analyzed with respect to frequency. Initially high ε' was found at low frequency which

gradually decreases as the frequency values reaches to higher level. Result of all samples well matches with the Koop's theory. This theory explains the structure of dielectrics. Furthermore, in accordance with Koop's theory ferrites are assumed to be including grain and grain boundaries. These two stratified structures have variation in its electrical property. Grains are reasonably crystalline part, therefore; electrical mobility is smoother. Whereas, grain boundaries have characteristic of separation between grains that hinder the costs. Thus, we have a tendency to get high impedance during this layer. At low frequency Maxwell Wagner interfacial polarization was determined, which is attributable to charge formation the boundaries of grains. This development is often seen altogether various polycrystalline materials. Whereas this property nonexistent at higher frequency as a result ε' values become constant.

3.4.2 Tangent loss and dielectric loss factor

It was determined that tangent loss (tan δ = 1/2πfRC) and material loss factor or imaginary part of a complex number of dielectric constant ($\varepsilon'' = \varepsilon' \tan \delta$) of all samples are analogous to ε'. Figures 11 and 12 show that the tangent loss and dielectric loss factor (ε'') values were higher at low frequency. Whereas, they decrease bit by bit with increase of frequency. Dependency of those values vanish at higher frequencies. Tangent loss is defined as it is that the measures of energy absorption within the material medium. High energy loss is probably going to correspond with low frequency

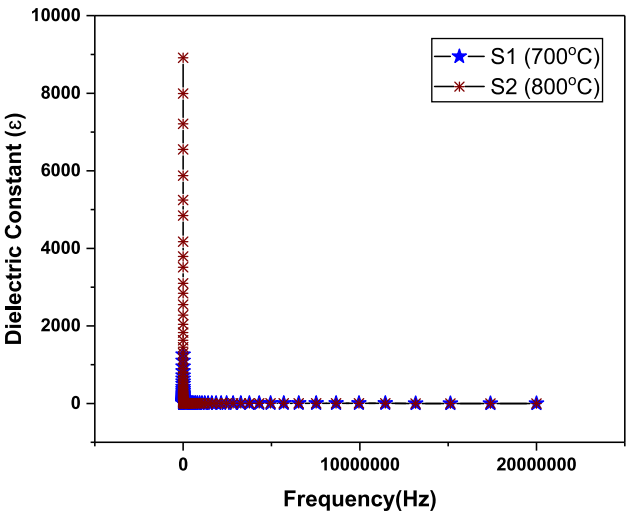

Figure 10: Variation in dielectric constant of samples calcined at 700 °C and 800 °C as a function of frequency.

because the determined result matches well with the Koop's phenomenological theory. Such loses are often explained by applied field and polarization resonance. At lower frequencies grain boundaries possesses higher impedance, therefore, movement of the lepton across the potential needed bigger energy that is reason of energy losses. Contrary to this, grains have lower resistance within the path lepton at high frequency operation since lesser energy loss depends upon energy demand [17].

3.4.3 AC conductivity

The AC conductivity was appraised as depicted in Eq. (4). Where, f, ε_o and ε'' are frequency, permittivity and imaginary part of dielectric constant or dielectric loss factor.

$$\sigma_{AC} = 2\pi f \varepsilon_0 \varepsilon'' \tag{4}$$

AC conductivity in relation to frequency (100 Hz–20 MHz) is shown in Figure 13. It was observed that the AC conductivity was increased with frequency.

3.5 Photocatalytic performance

The PCA of $MgFe_2O_4$ was appraised for MB dye and responses are depicted in Figures 14 and 15. The $MgFe_2O_4$ showed promising catalytic activity as revealed by

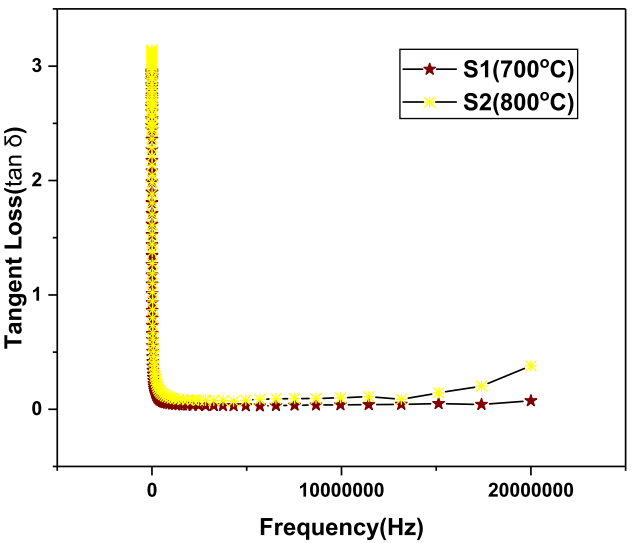

Figure 11: Tangent loss of samples calcined at 700 °C and 800 °C versus frequency.

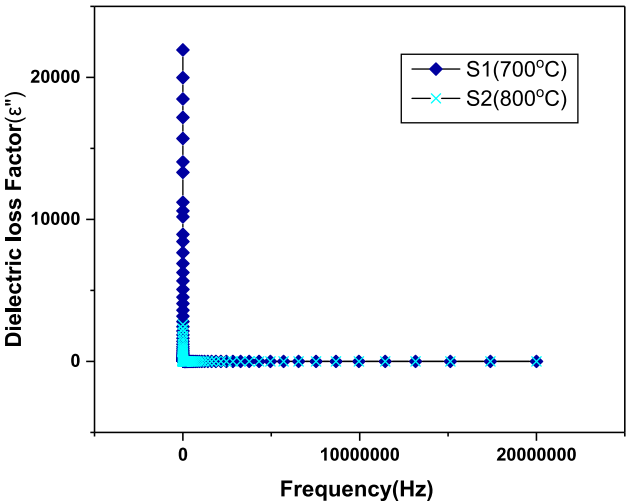

Figure 12: Variation in dielectric loss factor of samples calcined at 700 °C and 800 °C versus frequency.

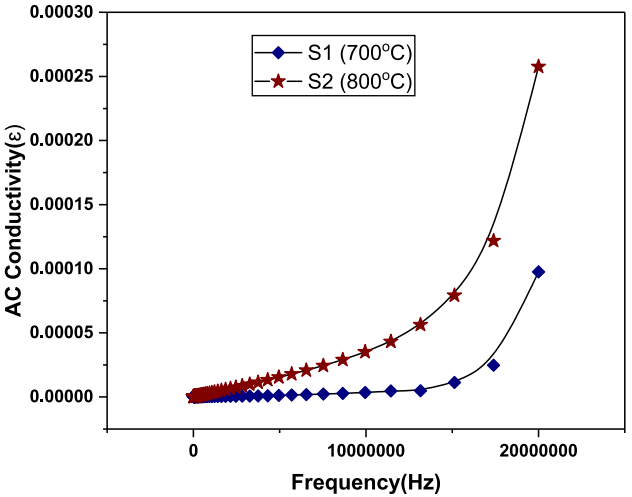

Figure 13: Variation in AC conductivity of samples calcined at 700 °C and 800 °C versus frequency.

the change in the dye absorption data versus irradiation time since the dye absorption peak decreased constantly, which revealed the destruction of dye structure to the degradation byproducts. Both catalyst dose and irradiation time affected the MB dye degradation and up to 78% dye degradation was achieved in 20 min of

irradiation, which revealed that the Mg ferrite is highly active catalyst. Degradation of MB dye takes place through oxidation and reduction processes on the surface of catalyst (Figure 16). Magnesium ferrites on irradiation excited and holes (h^+) and electron pair are produced, $^{\bullet}OH$ radicals are generated [31, 32]. Similarly, excess of electrons in conduction band are also converted into $^{\bullet}OH$. These radicals distort the structure of MB dye through oxidation and convert them into less toxic products such as H_2O and CO_2 [33]. Based on the PCA, it is concluded that the $MgFe_2O_4$ is highly active under visible light irradiation and could be employed for the treatment of effluents contains textile dyes, which is one of major issue of environmental pollution. These findings are also in agreement with previous reports that the ferrite NPs are active photocatalysts and have potential to degrade the pollutants, i.e., the photocatalytic efficiency of barium hexaferrite were studied and it was observed that the doping enhanced the PCA of $BaFe_{12}O_{19}$. The $BaFe_{12}O_{19}$ showed 64.23% of higher CV dye under visible light irradiation versus undoped sample [34]. Similarly, the manganese ferrite NPs were synthesized and PCA was studied for the degradation of MB dye. The $MnFe_2O_4$ furnished 99% MB dye degradation [35]. Hence, the $MgFe_2O_4$ could be employed for the remediation of dyes in textile wastewater, which is one of major environmental issue and this

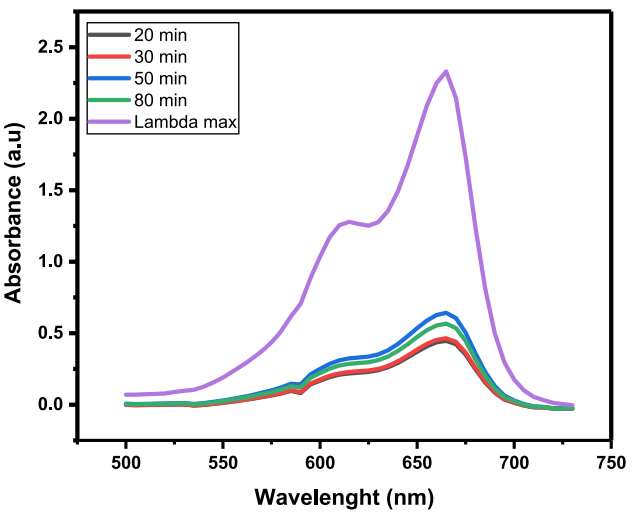

Figure 14: Absorbance as a function of wavelength for degradation of MB dye using 0.03 g of catalyst at different time intervals.

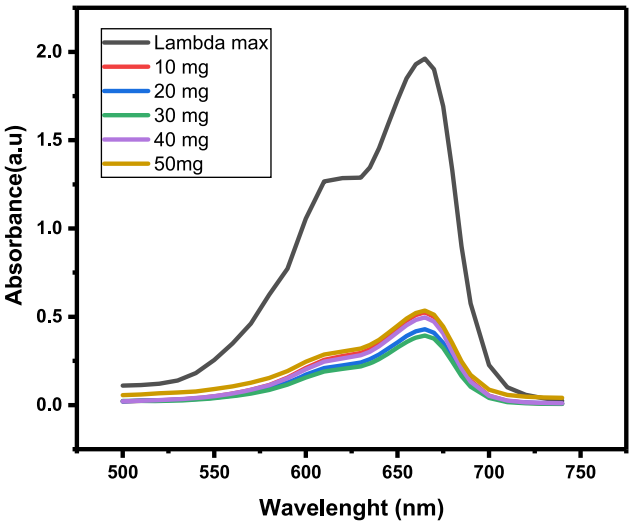

Figure 15: Absorbance as a function of wavelength for different photo-catalytic doses (0.01–0.05 g).

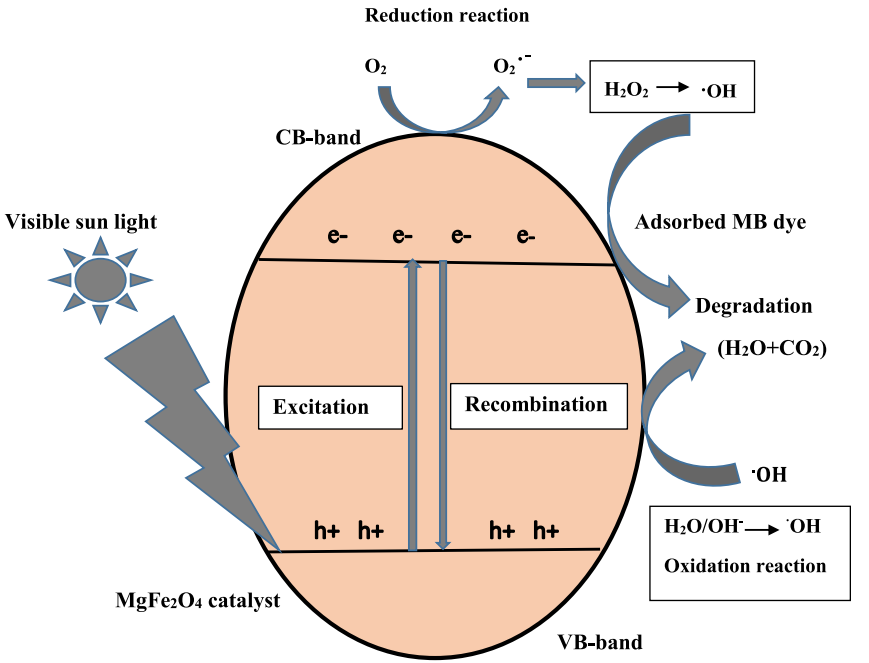

Figure 16: Mechanism of photocatalytic degradation of MB dye by magnesium ferrite.

pollution issue need to be addressed by developing innovative materials [12, 36–49] and efficient wastewater treatment approaches.

4 Conclusions

The $MgFe_2O_4$ NPs was prepared by sol-gel auto combustion approach. The formation of spinel cubic ferrites with higher crystallinity at 800 °C temperature (calcination) was observed. Particle size of $MgFe_2O_4$ was in the range of 45–55 nm. A frequency dependent dielectric property was studied and it was observed that tangent loss, dielectric constant and dielectric loss values were declined with frequency. The AC conductivity was enhanced as the frequency was increased that was due to increase in charge hopping. Temperature has considered effect on the particle size, cationic distribution, and composition and dielectric properties of the $MgFe_2O_4$ NPs. The PCA was appraised for MB dye removal under visible light irradiation and the $MgFe_2O_4$ annealed at 800 °C showed excellent degradation efficiency under visible light irradiation, which could possibly be used for the degradation of dyes in effluents.

Acknowledgments: The authors express their gratitude to Princess Nourah bint Abdulrahman University Researchers Supporting Project number (PNURSP2023R11), Princess Nourah bint Abdulrahman University, Riyadh, Saudi Arabia.
Author contributions: All the authors have accepted responsibility for the entire content of this submitted manuscript and approved submission.
Research funding: This research was funded by Princess Nourah bint Abdulrahman University Researchers Supporting Project number (PNURSP2023R11), Princess Nourah bint Abdulrahman University, Riyadh, Saudi Arabia.
Conflict of interest statement: The authors declare no conflicts of interest regarding this article.

References

1. Nazir A., Raza M., Abbas M., Abbas S., Ali A., Ali Z., Younas U., Al-Mijalli S. H., Iqbal M. Microwave assisted green synthesis of ZnO nanoparticles using Rumex dentatus leaf extract: photocatalytic and antibacterial potential evaluation. *Z. Phys. Chem.* 2022, *236*, 1203–1217.
2. Bukhari A., Atta M., Nazir A., Shahab M. R., Kanwal Q., Iqbal M., Albalawi H., Alwadai N. Catalytic degradation of MO and MB dyes under solar and UV light irradiation using ZnO fabricated using Syzygium Cumini leaf extract. *Z. Phys. Chem.* 2022, *236*, 659–671.
3. Gul N., Ata S., Bibi I., Azam M., Shahid A., Alwadai N., Masood N., Iqbal M. Size controlled synthesis of silver nanoparticles: a comparison of modified Turkevich and BRUST methods. *Z. Phys. Chem.* 2022, *236*, 1173–1189.

4. Bibi I., Ghulam T., Kamal S., Jilani K., Alwadai N., Iqbal M. Green synthesis of iron nanoparticles and photocatalytic activity evaluation for the degradation of methylene blue dye. *Z. Phys. Chem.* 2022, *236*, 1191–1201.
5. Nazir A., ur Rehman S., Abbas M., Iqbal D. N., Ahsraf A. R., Iqbal M. Green synthesis and characterization of copper nanoparticles using Parthenium hysterophorus extract: antibacterial and antioxidant activities evaluation. *Chem. Int.* 2022, *8*, 68–76.
6. Almessiere M., Slimani Y., Auwal I., Shirsath S., Gondal M., Sertkol M., Baykal A. Biosynthesis effect of Moringa oleifera leaf extract on structural and magnetic properties of Zn doped Ca–Mg nano-spinel ferrites. *Arab. J. Chem.* 2021, *14*, 103261.
7. Almessiere M., Slimani Y., El Sayed H., Baykal A. Ca^{2+} and Mg^{2+} incorporated barium hexaferrites: structural and magnetic properties. *J. Sol. Gel Sci. Technol.* 2018, *88*, 628–638.
8. Almessiere M. A., Slimani Y., Rehman S., Khan F. A., Sertkol M., Baykal A. Green synthesis of Nd substituted Co–Ni nanospinel ferrites: a structural, magnetic, and antibacterial/anticancer investigation. *J. Phys. Appl. Phys.* 2021, *55*, 055002.
9. Almessiere M., Slimani Y., Algarou N., Gondal M., Wudil Y., Younas M., Auwal I., Baykal A., Manikandan A., Zubar T. Electronic, magnetic, and microwave properties of hard/soft nanocomposites based on hexaferrite $SrNi_{0.02}Zr_{0.02}Fe_{11.96}O_{19}$ with variable spinel phase MFe_2O_4 (M = Mn, Co, Cu, and Zn). *Ceram. Int.* 2021, *47*, 35209–35223.
10. Almessiere M., Slimani Y., Gungunes H., Nawaz M., Al-ahmari F., Manikandan A., Baykal A. Investigation of the crystal/magnetic structure, magnetic and optical properties of $SrY_xNb_xFe_{12-2x}O_{19}$ ($x \leq 0.05$) hexaferrites. *Phys. Scripta* 2020, *95*, 055802.
11. Algarou N. A., Slimani Y., Almessiere M. A., Sadaqat A., Trukhanov A. V., Gondal M. A., Hakeem A. S., Trukhanov S. V., Vakhitov M. G., Klygach D. S. Functional $Sr_{0.5}Ba_{0.5}Sm_{0.02}Fe_{11\ 98}O_4/x(Ni_{0.8}Zn_{0.2}Fe_2O_4)$ hard–soft ferrite nanocomposites: structure, magnetic and microwave properties. *Nanomaterials* 2020, *10*, 2134.
12. Almessiere M. A., Slimani Y., Gungunes H., Manikandan A., Baykal A. Investigation of the effects of Tm^{3+} on the structural, microstructural, optical, and magnetic properties of Sr hexaferrites. *Results Phys.* 2019, *13*, 102166.
13. Paik J.-G., Lee M.-J., Hyun S.-H. Reaction kinetics and formation mechanism of magnesium ferrites. *Thermochim. Acta* 2005, *425*, 131–136.
14. Khan M. I., Touheed M., Sajjad-ul-Hasan M., Siddique M., Rouf S. A., Ahmad T., Fatima M., Iqbal M., Almoneef M. M., Alwadai N. Hydrothermal synthesis, characterization and photocatalytic activity of Mg doped MoS_2. *Z. Phys. Chem.* 2022, *236*, 155–168.
15. Ata S., Naz S., Bibi I., Mohsin I.-u., Islam A., Mehmood A., Al-Fawzan F. F., Alissa S. A., Iqbal M. Highly photosensitized $Mg_4\ Si_6O_{15}(OH)_2\ 6H_2O$@ guar gum nanofibers for the removal of methylene blue under solar light irradiation. *Z. Phys. Chem.* 2022, *236*, 181–196.
16. Pendyala S. K., Thyagarajan K., GuruSampath Kumar A., Obulapathi L. Effect of Mg doping on physical properties of Zn ferrite nanoparticles. *J. Aust. Ceram. Soc.* 2018, *54*, 467–473.
17. Majid F., Shahin A., Ata S., Bibi I., Malik A., Ali A., Laref A., Iqbal M., Nazir A. The effect of temperature on the structural, dielectric and magnetic properties of cobalt ferrites synthesized via hydrothermal method. *Z. Phys. Chem.* 2021, *235*, 1279–1296.
18. Mohammad A., Aliridha S., Mubarak T. Structural and magnetic properties of mg-co ferrite nanoparticles. *Digest J. Nanomater. Biostruct.* 2018, *13*, 615–623.
19. Salem N. M., Awwad A. M. Green synthesis and characterization of ZnO nanoparticles using Solanum rantonnetii leaves aqueous extract and antifungal activity evaluation. *Chem. Int.* 2022, *8*, 12–17.
20. Naseer A., Iqbal M., Ali S., Nazir A., Abbas M., Ahmad N. Green synthesis of silver nanoparticles using Allium cepa extract and their antimicrobial activity evaluation. *Chem. Int.* 2022, *8*, 89–94.

21. Naseri M. G., Saion E. B., Ahangar H. A., Shaari A. H., Hashim M. Simple synthesis and characterization of cobalt ferrite nanoparticles by a thermal treatment method. *J. Nanomater.* 2010, *2010*, 75.
22. Maensiri S., Sangmanee M., Wiengmoon A. Magnesium ferrite ($MgFe_2O_4$) nanostructures fabricated by electrospinning. *Nanoscale Res. Lett.* 2009, *4*, 221.
23. Jacobs I. High field magnetization study of ferrimagnetic arrangements in chromite spinels. *J. Phys. Chem. Solid.* 1960, *15*, 54–65.
24. Shammout M. W., Awwad A. M. A novel route for the synthesis of copper oxide nanoparticles using Bougainvillea plant flowers extract and antifungal activity evaluation. *Chem. Int.* 2021, *7*, 71–78.
25. Amer M. W., Awwad A. M. Green synthesis of copper nanoparticles by *Citrus limon* fruits extract, characterization and antibacterial activity. *Chem. Int.* 2021, *7*, 1–8.
26. Mohammad A. M., Ridha S. M. A., Mubarak T. H. Dielectric properties of Cr-substituted cobalt ferrite nanoparticles synthesis by citrate-gel auto combustion method. *Int. J. Appl. Eng. Res.* 2018, *13*, 6026–6035.
27. Sundari R., Hua T. I., Aziz M., Nizar D. The characterization study of ferrites (magnesium and manganese) using sol gel method. *Malays. J. Anal. Sci.* 2014, *18*, 485–490.
28. Awwad A. M., Amer M. W., Salem N. M., Abdeen A. O. Green synthesis of zinc oxide nanoparticles (ZnO–NPs) using Ailanthus altissima fruit extracts and antibacterial activity. *Chem. Int.* 2020, *6*, 151–159.
29. Awwad A. M., Amer M. W. Biosynthesis of copper oxide nanoparticles using Ailanthus altissima leaf extract and antibacterial activity. *Chem. Int.* 2020, *6*, 210–217.
30. Dar M. A., Batoo K. M., Verma V., Siddiqui W., Kotnala R. Synthesis and characterization of nano-sized pure and Al-doped lithium ferrite having high value of dielectric constant. *J. Alloys Compd.* 2010, *493*, 553–560.
31. Qureshi K., Ahmad M. Z., Bhatti I. A., Zahid M., Nisar J., Iqbal M. Graphene oxide decorated $ZnWO_4$ architecture synthesis, characterization and photocatalytic activity evaluation. *J. Mol. Liq.* 2019, *285*, 778–789.
32. Ashar A., Iqbal M., Bhatti I. A., Ahmad M. Z., Qureshi K., Nisar J., Bukhari I. H. Synthesis, characterization and photocatalytic activity of ZnO flower and pseudo-sphere: nonylphenol ethoxylate degradation under UV and solar irradiation. *J. Alloys Compd.* 2016, *678*, 126–136.
33. Iqbal M., Bhatti I. A. Gamma radiation/H_2O_2 treatment of a nonylphenol ethoxylates: degradation, cytotoxicity, and mutagenicity evaluation. *J. Hazard Mater.* 2015, *299*, 351–360.
34. Bibi I., Muneer M., Iqbal M., Alwadai N., Almuqrin A. H., Altowyan A. S., Alshammari F. H., Almuslem A. S., Slimani Y. Effect of doping on dielectric and optical properties of barium hexaferrite: photocatalytic performance under solar light irradiation. *Ceram. Int.* 2021, *47*, 31518–31526.
35. Ata S., Shaheen I., Majid F., Bibi I., Jilani K., Slimani Y., Iqbal M. Hydrothermal route for the synthesis of manganese ferrite nanoparticles and photocatalytic activity evaluation for the degradation of methylene blue dye. *Z. Phys. Chem.* 2021, *235*, 1433–1445.
36. Elsherif K. M., Alzalouk Z. Y., Zubi A., Al-Ddarwish S. A.-S. Facile spectrophotometric determination of Cd (II) and Pb (II) using murexide reagent in mixed solvent system. *Chem. Int.* 2022, *8*, 144–152.
37. Alahmari F., Rehman S., Almessiere M., Khan F. A., Slimani Y., Baykal A. Synthesis of $Ni_{0.5}Co_{0.5-x}Cd_xFe_{1.78}Nd_{0.02}O_4$ ($x \leq 0.25$) nanofibers by using electrospinning technique induce anti-cancer and anti-bacterial activities. *J. Biomol. Struct. Dyn.* 2021, *39*, 3186–3193.
38. Awwad A. M., Amer M. A. Adsorption of Pb(II), Cd(II), and Cu(II) ions onto SiO_2/kaolinite/Fe_2O_3 composites: modeling and thermodynamics properties. *Chem. Int.* 2022, *8*, 95–100.
39. Sasmaz M., Senel G. U., Obek E. Boron bioaccumulation by the dominant macrophytes grown in various discharge water environments. *Bull. Environ. Contam. Toxicol.* 2021, *106*, 1050–1058.

40. Ajeesha T., Ashwini A., George M., Manikandan A., Mary J. A., Slimani Y., Almessiere M., Baykal A. Nickel substituted $MgFe_2O_4$ nanoparticles via co-precipitation method for photocatalytic applications. *Phys. B Condens. Matter* 2021, *606*, 412660.
41. Abbas N., Hussain N., Gohar U. F., Zaheer F., Hamza M., Yasir M., Abbas A. Potential applications of indigenous bacterial consortium for the treatment of textile effluents and condition optimization by RSM technique. *Chem. Int.* 2022, *8*, 114–129.
42. Idika D., Ndukwe N., Ogukwe C. Appraisal of bed height and flow rate effect on the removal of dyes on Pine biomass. *Chem. Int.* 2022, *8*, 42–46.
43. Sasmaz A., Sasmaz B., Hein J. R. Geochemical approach to the genesis of the Oligocene-stratiform manganese-oxide deposit, Chiatura (Georgia). *Ore Geol. Rev.* 2021, *128*, 103910.
44. Chokor A. A., Achugwo C. N. Distribution, source identification and eco-toxicological risks of PAHs in sediments of Aba River at Ogbor-Hill region, Nigeria. *Chem. Int.* 2022, *8*, 47–57.
45. Ukpaka C. P., Ugiri A. C. Biodegradation kinetics of petroleum hydrocarbon in soil environment using Mangnifera indica seed biomass: a mathematical approach. *Chem. Int.* 2022, *8*, 77–88.
46. Sasmaz M., Senel G. U., Obek E. Strontium accumulation by the terrestrial and aquatic plants affected by mining and municipal wastewaters (Elazig, Turkey). *Environ. Geochem. Health* 2020, *43*, 1–14.
47. Akhtar S., Rehman S., Almessiere M. A., Khan F. A., Slimani Y., Baykal A. Synthesis of $Mn_{0.5}Zn_{0.5}Sm_xEu_xFe_{1.8-2x}O_4$ nanoparticles via the hydrothermal approach induced anti-cancer and anti-bacterial activities. *Nanomaterials* 2019, *9*, 1635.
48. Nazir A., Zahid S., Mahmood Z., Kanwal F., Latif S., Imran M., Hassan F., Iqbal M. Adsorption kinetics for the removal of toxic Congo red dye by polyaniline and citrus leaves as effective adsorbents. *Z. Phys. Chem.* 2022, *236*, 1301–1319.
49. Ali F., Hamza M., Iqbal M., Basha B., Alwadai N., Nazir A. State-of-art of silver and gold nanoparticles synthesis routes, characterization and applications: a review. *Z. Phys. Chem.* 2022, *236*, 291–326.